Performance comparison of aperture codes for multimodal, multiplex spectroscopy

Ashwin A. Wagadarikar, Michael E. Gehm, and David J. Brady*

Duke University Fitzpatrick Institute for Photonics, Box 90291, Durham, North Carolina 27708, USA

*Corresponding author: dbrady@duke.edu

We experimentally evaluate diverse static independent column codes in a coded aperture spectrometer. The performance of each code is evaluated based on the signal-to-noise ratio (SNR), defined as the peak value in the spectrum to the standard deviation of the background noise, as a function of subpixel vertical misalignments. Among the code families tested, an S-matrix-based code produces spectral reconstructions with the highest SNR. The SNR is least sensitive to vertical subpixel misalignments on the detector with a Hadamard-matrix-based code. Finally, the increased sensitivity of a spectrometer using a coded aperture instead of a slit is demonstrated. © 2007 Optical Society of America

   OCIS codes: 120.6200, 300.6190.

1. Introduction

In a traditional slit spectrometer, the internal relay optics and the dispersive element function together to produce multiple shifted images of a slit input aperture at wavelength-dependent locations at the detector plane. Being able to spatially distinguish these locations on the detector determines the spectral resolution of the instrument. In particular, if the pixel pitch is significantly smaller than the width of the slit, the spectral width of a resolution element on the detector is directly proportional to the slit width. Thus, achieving good spectral resolution requires a narrow slit width [1]. Unfortunately, limiting the slit width also restricts the light throughput, or étendue, of the instrument.

   This trade-off between spectral resolution and light throughput poses an important challenge to the use of slit spectrometers for the spectral characterization of weak, diffuse sources, i.e., sources producing an optical field that is large in both spatial and angular extent.

   A more effective instrument for spectroscopy of weak, diffuse sources calls for a design that maximizes the photon collection efficiency of the instrument without sacrificing any spectral resolution. We have previously reported on the development of a new class of coded aperture spectrometer known as the static, multimodal, multiplex spectrometer (MMS) [2]. This design addresses the problem of spectroscopy of weak, diffuse sources by replacing the input slit on the aperture of a traditional slit spectrometer with a coded pattern. The design has also demonstrated success in detecting Raman peaks of ethanol in a tissue phantom, a weak, diffuse source of Raman photons [3].

   In a slit spectrometer, the intensity profile on the detector plane is a direct estimate of the spectral density at the slit input aperture [4]. In contrast, our coded aperture spectrometer is an example of a computational sensor, because postprocessing of the detector measurements is required to generate an estimate of the spectral density. Uniform input illumination of the code pattern on the aperture produces an output intensity distribution on the detector that is, to first approximation, a convolution of the input aperture pattern and the spectrum of the source. Thus, each spectral peak of the source in the spectral range of the instrument will result in an image of the aperture on the detector. If two peaks are close enough to each other, the corresponding aperture images overlap.

   This overlap implies that light falling on a given column of the detector can arise from a combination of different wavelengths passing through different locations on the input aperture. To break this ambi-

guity and eventually determine the spectral content of the light source, a well-designed aperture code is required. In a previous paper [2], we presented the general mathematical framework for developing an aperture code that allows us to estimate the mean spectrum across an extended aperture. That paper demonstrates the appeal of using independent column codes as aperture mask patterns for dispersive spectroscopy. In particular, it identifies discrete codes based on the Hadamard and S-matrix families [5] and continuous codes based on the harmonic and Legendre families as codes of interest for further study.

Here, we experimentally evaluate each of these codes for their effect on the spectral estimation performance of a test-bed static MMS instrument. To this end, this work has two major objectives:

1. To determine which of the studied aperture codes maximizes the signal-to-noise ratio (SNR) of the spectral estimate from the instrument, where the SNR is defined as the ratio of the peak value in the spectrum to the standard deviation of the background noise.

2. To find the aperture code that is least sensitive to subpixel vertical misalignments with respect to the detector. These misalignments are essentially a result of the blurring and the nonunity vertical magnification in the optical system. Such distortions imply that the mask features, whose feature sizes are integral multiples of the charge-coupled device (CCD) pixel size, are imaged to a nonintegral number of CCD pixels, thus opening up the possibility for vertical subpixel misalignments to be present immediately after manufacturing of the instrument.

What follows is a description of the different aperture codes investigated. Section 3 presents the system description. Section 4 describes the inversion algorithm used to reconstruct a spectrum of a given source when an independent column code is used as the aperture pattern of the static MMS instrument. Section 5 describes the process of developing a system forward model that helps improve the accuracy of the spectral estimates from the instrument. Section 6 explains the SNR metric used to evaluate the quality of a spectral estimate. Finally, Section 7 describes the experimental method and presents experimental results that (i) compare the performance of our instrument with the various aperture codes and (ii) demonstrate the increased sensitivity of a coded aperture spectrometer over a slit spectrometer.

2. Aperture Codes

Each independent column aperture code in this study is designed so that each column in the code has a width of 54 μm, six times the width of the CCD pixels.

A. Discrete Independent Column Codes

1. Shuffled order-48 S-matrix with dead rows (see Fig. 1). This code is an order-48 S-matrix shifted and scaled to have values in the interval [0,1]. The rows

Fig. 1. Shuffled order-48 S-matrix with dead rows (3456 μm tall, 2592 μm wide).

and columns are shuffled in a random, but reproducible, way to avoid spurious correlations that have been observed in the past [3]. Each mask row is six CCD pixels tall and two dead rows are added between mask rows to reduce cross talk between adjacent codes resulting from the point-spread function.

2. Shuffled order-48 S-matrix without dead rows (see Fig. 2). This code is similar to code 1, except each mask row is eight CCD pixels tall and there are no dead rows.

Fig. 2. Shuffled order-48 S-matrix without dead rows (3456 μm tall, 2592 μm wide).

Fig. 3. Shuffled, row-doubled order-24 Hadamard with dead rows (3456 μm tall, 1296 μm wide).

3. *Shuffled, row-doubled order-24 Hadamard with dead rows* (see Fig. 3). To create this code, the rows and columns of an order-24 Hadamard code are shuffled. Then each row of the resulting matrix, $\mathbf{H}(m, :)$, is row doubled so that it is replaced with two rows, the primary and complementary rows:

$$\mathbf{H}(m, :) \rightarrow \begin{bmatrix} \frac{1}{2}(1 + H(m, :)) \\ \frac{1}{2}(1 - H(m, :)) \end{bmatrix}. \qquad (1)$$

Each mask row is six CCD pixels tall, and two dead rows are added between mask rows.

4. *Shuffled, row-doubled order-24 Hadamard without dead rows* (see Fig. 4). This code is similar to code 3, except each mask row is eight CCD pixels tall and there are no dead rows.

5. *Shuffled, row-doubled, stacked order-24 Hadamard with dead rows* (see Fig. 5). This code is similar to code 3, except the code is arranged so that all the primary rows after row doubling are placed above all the complementary rows.

6. *Shuffled, row-doubled, stacked order-24 Hadamard without dead rows* (see Fig. 6). This code is similar to code 5, except each mask row is eight CCD pixels tall and there are no dead rows.

B.   Continuous Independent Column Codes

7. *Half-toned harmonic* (see Fig. 7). This aperture code is a collection of code columns, where the code in column m is given by

Fig. 4. Shuffled, row-doubled order-24 Hadamard without dead rows (3456 μm tall, 1296 μm wide).

$$T_x \in \left\{ \frac{1}{2}\left(1 + \cos\left(m\,\frac{y\pi}{Y}\right)\right) \right\}, \quad m \in [0, \ldots, 48]. \qquad (2)$$

These cosine-based codes are shifted and scaled to have values in the interval [0, 1]. The continuous-tone codes are converted to half-toned versions by subdividing each element in the continuous-tone pattern to a randomly shuffled array of 0's and 1's such

Fig. 5. Shuffled, row-doubled, stacked order-24 Hadamard with dead rows (3456 μm tall, 1296 μm wide).

Fig. 6. Shuffled, row-doubled, stacked order-24 Hadamard without dead rows (3456 μm tall, 1296 μm wide).
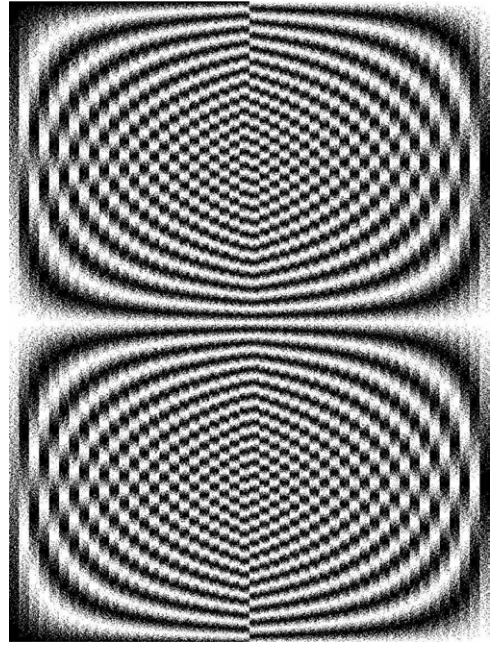

Fig. 8. Half-toned, reordered harmonic (3456 μm tall, 2592 μm wide).

that the net transmission of this array matches the gray-scale value of the continuous-tone pattern.

8. Half-toned, reordered harmonic (see Fig. 8). This code is similar to code 7, except all the even columns are placed to the right of the odd columns.

9. Half-toned Legendre (see Fig. 9). This aperture code is a collection of code columns, where the code in column *m* is given by

$$T_x \in \left\{ \frac{1}{2}\left(1 + P_m\left(\frac{y}{\overline{Y}}\right)\right)\right\}, \quad m \in [0, \ldots, 48], \quad (3)$$

$$P_m(y) = \frac{1}{2^m} \sum_{n=0}^{\lfloor m/2 \rfloor} (-1)^n \binom{m}{n}\binom{2m-2n}{m} y^{m-2n}. \quad (4)$$

10. Half-toned, reordered Legendre (see Fig. 10). This code is similar to code 9, except all the even columns are placed to the right of the odd columns.
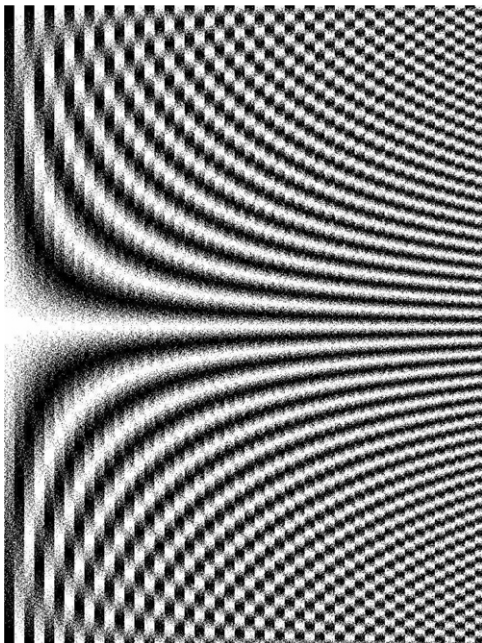

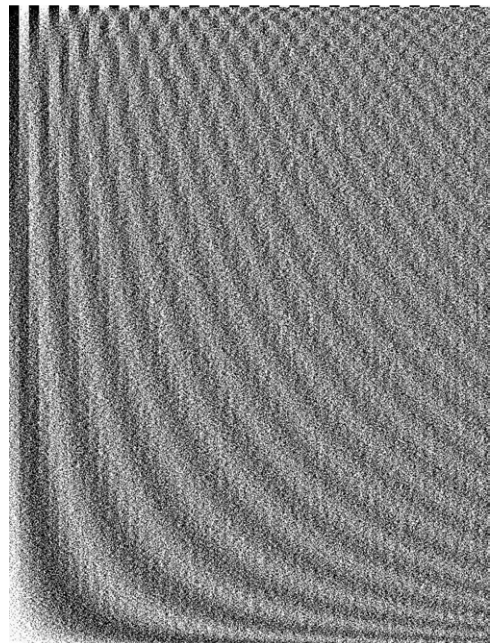Fig. 7. Half-toned harmonic (3456 μm tall, 2592 μm wide).

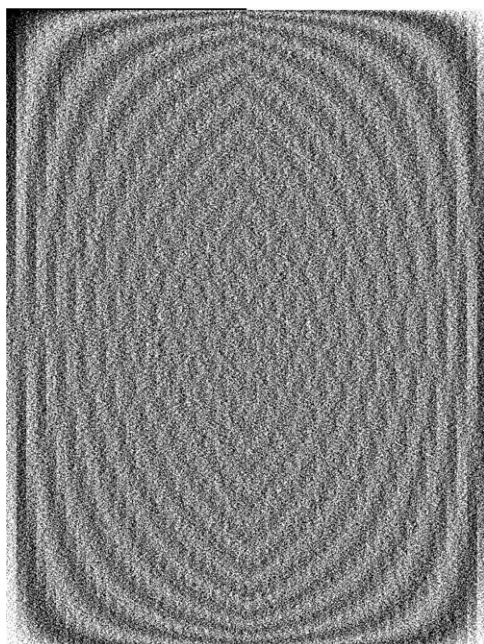Fig. 9. Half-toned Legendre (3456 μm tall, 2592 μm wide).

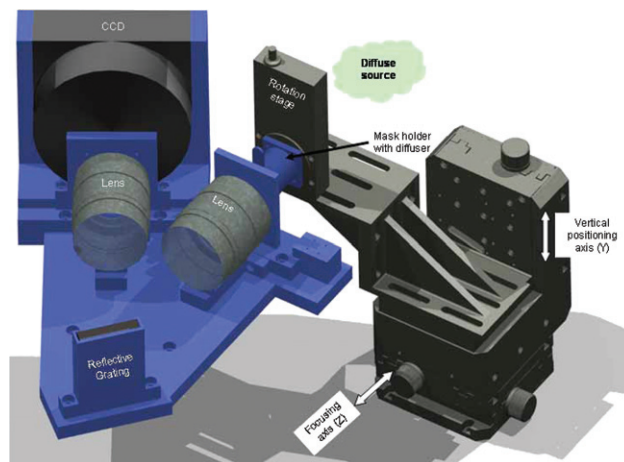Fig. 10. Half-toned, reordered Legendre (3456 µm tall, 2592 µm wide).

Fig. 11. (Color online) Experimental setup used to test the performance of a static multimodal multiplex coded aperture spectrometer with different aperture codes. Each aperture code mask is placed and secured inside the mask holder. The rotation stage allows rotational alignment of the mask images on the CCD. The two-axis translation stage provides control over the vertical sub-pixel misalignments of the mask images on the CCD and allows proper positioning of the mask along the optical axis to ensure that the mask images are in focus.

Since most CCDs are wider than they are tall, the limiting factor in designing a code for such a spectrometer is the number of rows that are imaged on the CCD. The different codes were chosen so that they occupy the same number of CCD rows. Thus, some code patterns were narrower than the rest.

In addition to these column-coded apertures, a slit aperture (36 µm width) was also tested as part of an experiment to demonstrate the improvement in the sensitivity of the instrument when a coded aperture is used.

3. System Description

Each aperture code is lithographically patterned on a chrome-on-quartz mask. In all the experiments, the spectral source used to test the performance of the spectrometer was a xenon discharge lamp (xenon Pen-Ray from UVP, LLC), chosen for its sharp spectral features corresponding to atomic transitions of the gas molecules. The spectrometer is a 4-f optical system consisting of two lenses (Pentax B7514C) that are focused at infinity, a volume holographic reflective grating with 1200 lines/mm used to disperse the incident light into multiple spectral channels, and a CCD with a 765×510 array of 9 µm square pixels (ST-7XMEI from SBIG, Inc.) chosen as the detector for its high performance/price ratio.

Figure 11 illustrates the experimental setup. Light from a weak, diffuse source, a xenon discharge lamp in this case, is incident on an engineered diffuser (Thorlabs, Inc.) and the transmitted light is incident directly on the coded aperture mask. Light transmitted through the mask passes through a Pentax lens and is subsequently dispersed into multiple spectral channels by the reflective grating. The spectral chan-

nels are imaged onto the CCD through the second Pentax lens.

Since the experimental method required control over the position of the aperture code mask, a mount was created to hold the mask and the diffuser, with the mask placed in front of the diffuser. The mask holder was mounted on a motorized rotation stage that was in turn mounted on a motorized two-axis translation stage. One of the axes (Y-axis) was perpendicular to the optical axis and was used for vertical positioning of the masks, while the other (Z-axis) was parallel to the optical axis and was used to position the mask so that the image observed on the CCD would be in focus.

For all the experiments, the CCD integration time was 700 ms. The spectrometer was found to have a spectral range of ~860–930 nm and an overall $f/\#$ of 3.7.

An example of a raw CCD measurement is shown in Fig. 12. The xenon spectrum has four major peaks in the spectral range of the instrument, as demonstrated by the four overlapping mask images of the aperture code on the CCD. The color bar indicates the interval that the pixel values attain after analog-to-digital conversion by the detector. The blurring caused by the point-spread function of the optical system is obvious. Demagnification of the aperture pattern horizontally and vertically is not obvious but is present. Imaging the aperture with the grating results in an image that is curved in the direction of dispersion [6]. This curvature, known as the smile distortion, is also visible. It can be corrected by fitting a second-order polynomial to the bright edge of the mask image and applying horizontal shifts to each row to straighten the mask images.
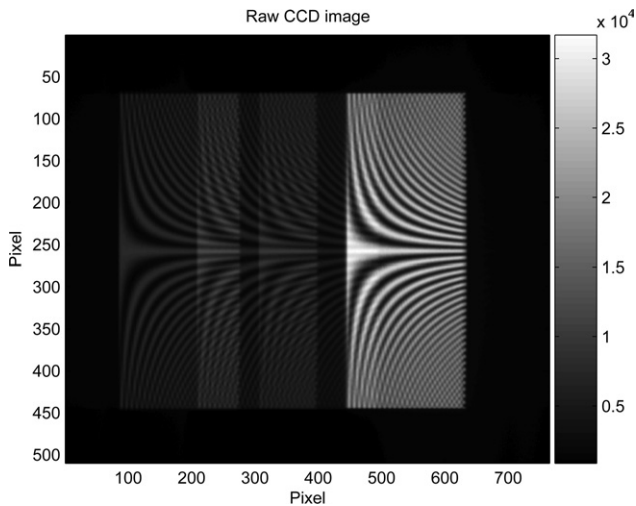
Fig. 12. Example of raw CCD data from the MMS spectrometer.

4. Inversion Algorithm

To first approximation, the image is a convolution of the aperture code with the source spectrum over the spectral range of the instrument. This can be represented as

$$(A)_{X \times Y}(S)_{Y \times Z} = (C)_{X \times Z}, \qquad (5)$$

where A is a matrix representing the input aperture code with X rows and Y independent columns, S is a matrix whose Y rows represent the spectra at the Y columns of the input aperture, and C is the data matrix containing the counts from the CCD. The spectral estimates in the rows of S have shifted spectral origins, reflecting the shifted input positions on the aperture mask.

To invert C to get S, a nonnegative least-squares (NNLS) algorithm [7,8] is used since photon counts are always positive. The algorithm to find S can be described as follows:

$$\arg \min_{x} |Mx - C_i|^2, \quad x \geq 0, \qquad (6)$$

where M is the spectral decoding matrix representing the coding scheme implemented in the spectrometer, x is a column of the S matrix with nonnegative elements, and C_i is a column from the data matrix C, $i \in [1, \ldots, Y]$. The algorithm is repeated over all columns of C to get all columns of S. Heuristically, this problem can be viewed as a situation in which the algorithm considers every column on the CCD and attempts to determine the contribution of photons from each column in the code, ultimately resulting in the spectral estimate matrix S.

We note that M is not the ideal independent column code that is printed on the aperture code mask [A as in Eq. (5)], but a pattern representing the physical coding scheme implemented as light propagates through the spectrometer. The construction of this M matrix is explained in greater detail in the following section.

5. Forward Model Development

As mentioned earlier, representing a measurement on the detector as a convolution between the input aperture code and the spectrum is only an approximation. In reality, the optical field is distorted in the form of (1) blurring and magnification as a result of diffraction and the lenses, (2) the smile distortion as a result of the grating and, (3) subpixel misalignments as a result of the mask being imaged to a nonintegral number of pixels vertically.

A forward model provides a physical description of the measurement process as well as a numerical simulation [9]. Derivation of relevant physical parameters describing the process can be used as a part of the data retrieval system [10]. In this case, the goal of developing a forward model is to simulate what is physically happening to the optical field in the spectrometer and thus estimate the actual coding scheme applied to the light after transmission through the coded input aperture. As will be demonstrated later in this section, incorporating knowledge of the estimated coding scheme into the spectral decoding matrix M produces less-noisy spectral reconstructions by the NNLS inversion algorithm than if one were to assume that $M = A$, the ideal independent column code that is printed on the aperture mask.

A forward model simulation of light propagation through the instrument allows us to estimate four physical parameters and one system parameter. The four physical parameters to be modeled are vertical blur, horizontal blur, vertical demagnification, and horizontal demagnification. The system parameter to be modeled is the vertical subpixel misalignment of the mask images on the CCD.

Note that in separating the blur and magnifications into horizontal and vertical components, the point-spread function of the system is assumed to be a Gaussian function separable in two dimensions that is uniform all over the detector. Further work, outside the scope of this paper, would be required to study the effect of modeling a spatially varying point-spread function across the detector.

Figure 13 highlights the steps in generating a MATLAB simulation of what is observed on the CCD. The simulation begins by starting with the the ideal aperture code matrix. This matrix is expanded vertically so that every element in the original aperture code matrix is represented by 20 simpixels vertically. There are two simpixels per subpixel. This generates a high-resolution representation of the optical field in the row dimension. Vertical demagnification through the optical system is simulated by interpolating each column in the matrix from the previous step. The resulting matrix is expanded horizontally so that every element in the matrix is represented by 20 simpixels horizontally. This generates a high-resolution representation of the optical field in the column dimension. Horizontal demagnification through the optical system is simulated by interpolating each row in the matrix from the previous step. Vertical blurring is simulated on this matrix by convolving each column with a
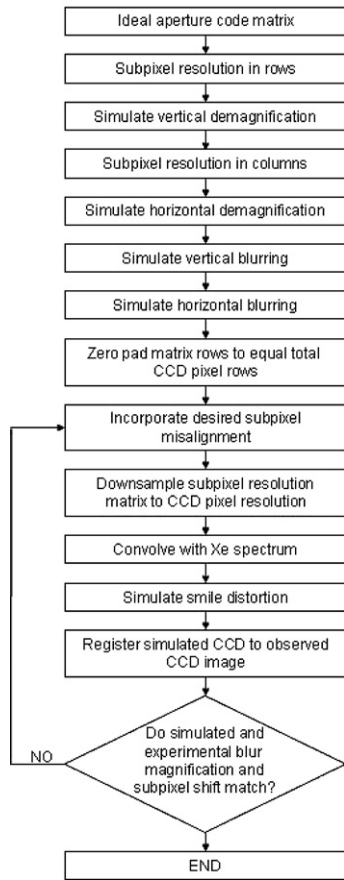
Fig. 13.   Foward model development flow chart.

Fig. 14.   Comparing the raw and simulated CCD images.

Gaussian. Then, horizontal blurring is simulated by convolving each row in the matrix with a Gaussian. At this point, the simulation accounts for the four physical parameters to be determined.

Since there are 510 rows on the CCD, the number of rows in this matrix is increased to 10,200 simpixel rows (510 × 20) by zero padding. This matrix is circularly shifted vertically by a variable amount corresponding to the desired subpixel misalignment (up to a shift of one full CCD pixel, i.e., 20 simpixels). The resulting matrix is downsampled to pixel resolution by grouping the rows and columns in the optical field representation into groups of 20. At this point, the simulation models the four physical parameters and the system parameter.

Smile distortion is simulated by shifting each row in the matrix from the previous step by fitting a second-order polynomial to the right edge of the mask pattern on the observed CCD image. Image registration is used to register the simulated CCD image with the observed CCD image, allowing for comparison between the two images.

This procedure is repeated with different subpixel shifts to find the shift that best matches the experimentally recorded CCD image. Figure 14 shows a comparison between observed and simulated CCD images.

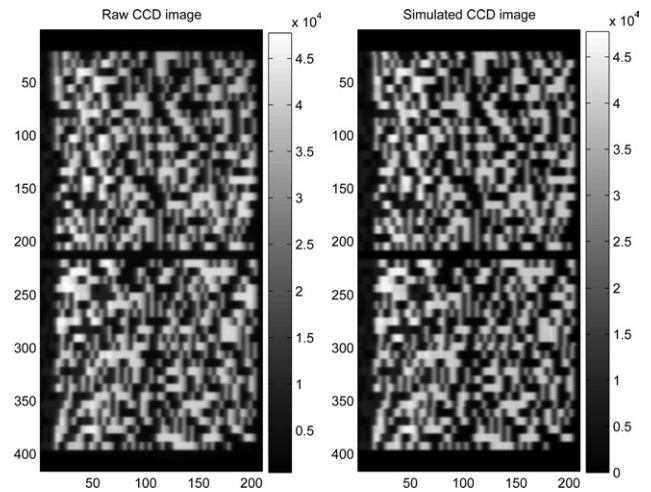To ensure that the simulation has sufficiently modeled the subpixel misalignment, comparisons of pixel intensities at the level of individual rows of pixels has to be performed at the top and bottom of the observed and simulated CCD images. Figure 15 demonstrates such a comparison between the observed and simulated CCD images by zooming in to rows at the top and bottom of both images.

The parameters for the blur, demagnification, and vertical subpixel misalignment from the forward model development can be used to generate a spectral decoding matrix, M, for the NNLS algorithm that represents the physical coding scheme applied to the light as it propagates through the spectrometer. The steps to generate the decoding matrix are identical to steps 1 through 10 in the procedure stated above for generating the forward model simulation.

Figure 16 demonstrates the transformation of the ideal decoding matrix to a forward modeled version that incorporates information about the blur, demagnification, and subpixel misalignment.
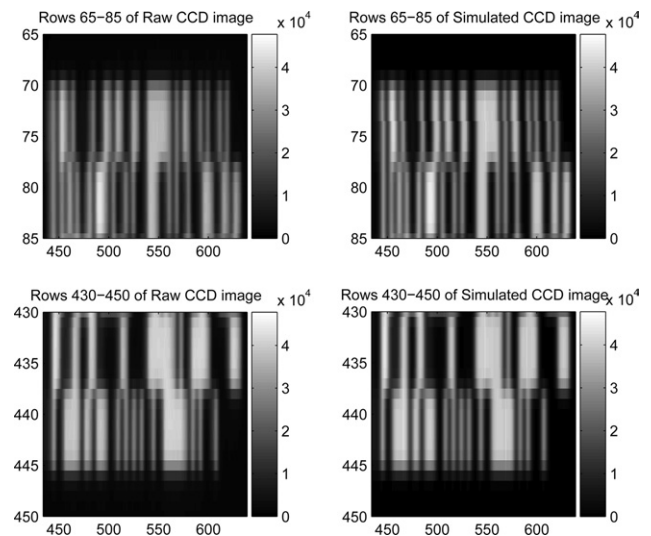

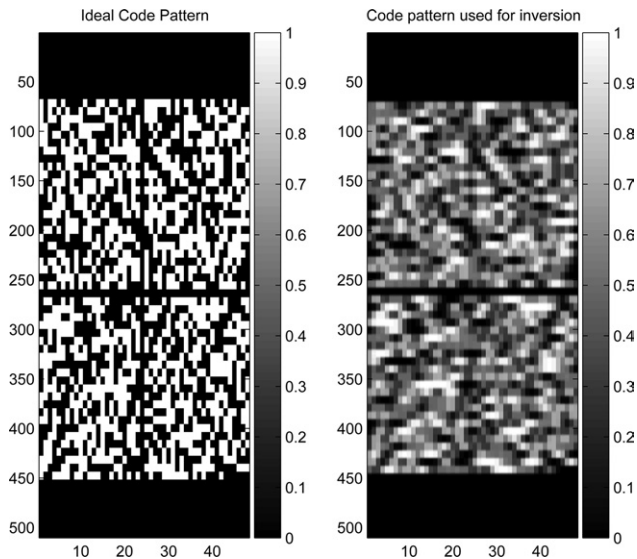Fig. 15.   Comparing the raw and simulated CCD images at the pixel level.

Fig. 16. Comparing the ideal coding scheme to the coding scheme determined to be physically implemented in the spectrometer through forward model development.

Figure 17 plots spectral reconstructions that demonstrate the effect of the forward model development. The thick solid curve is a spectral reconstruction with a forward-modeled decoding matrix. The other curve is a spectral reconstruction assuming the spectral decoding matrix is the same as the code printed on the aperture mask. The peaks in this spectrum are much lower than those in the spectrum generated after forward model development. Furthermore, there is a lot more noise around the peaks.

It is important to note that the technique of developing the forward model to improve spectral quality requires a source that behaves as a collection of quasimonochromatic sources. An example of such a
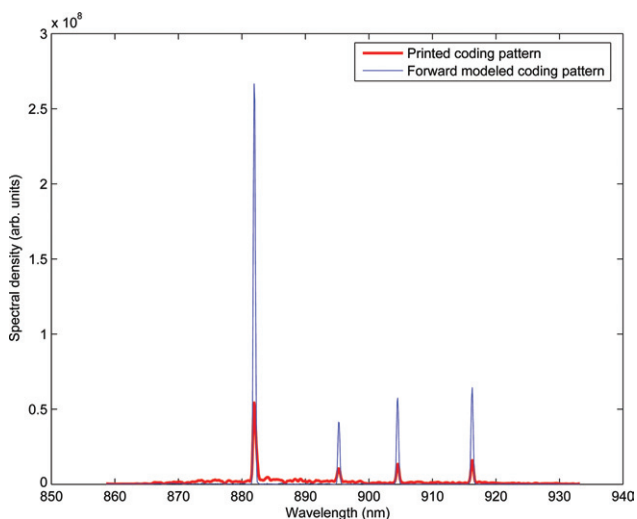

Fig. 17. (Color online) Spectral estimate before and after forward model development. Note that the spectral peaks are dramatically enhanced when the system is inverted using the coding matrix generated by the forward model, rather than the basic pattern printed on the aperture mask.
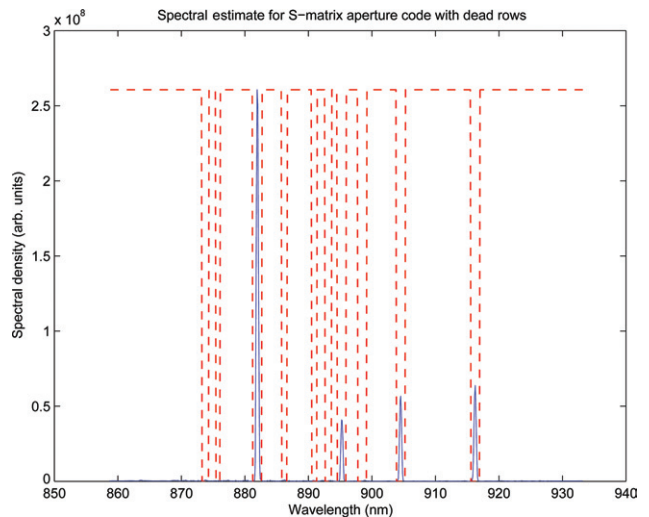

Fig. 18. (Color online) Sample spectral estimate and the noise mask (dashed line) used to evaluate the SNR of the spectral estimate.

source is a gas discharge lamp with sharp lines in the spectral range of the instrument, such as the xenon lamp used in this study. The technique should be viewed as a calibration tool for the spectrometer. Thus, one would build the optimal spectral decoding matrix based on the alignment and positioning of the mask images produced by a source with strong, sharp spectral features, such as the xenon lamp, before using it to reconstruct the spectrum of an arbitrary source.

6. Evaluating the Quality of a Spectral Estimate

Figure 18 is an example of a spectrum reconstructed for the S-matrix aperture code with dead rows. The dashed line is the noise mask, which is nonzero only in regions of the spectrum where there are no xenon peaks, thus classifying any reconstructed signal as noise.

To evaluate the quality of the reconstruction, the SNR for the spectral estimate is defined as

$$\text{SNR} = \frac{\text{peak value of the spectrum}}{\sigma \text{ of background noise under the noise mask}}.$$

(7)

The higher the SNR, the more accurate the spectral reconstruction is assumed to be.

7. Laboratory Experiments

A. Experimental Method

Before collecting any data, the mask with the aperture code had to be properly aligned and well focused on the CCD. MATLAB scripts were developed for computer control of both motorized stages and to acquire images from the CCD at specified exposure times. Once a mask was inserted into the mask holder, the rotational stage was adjusted to ensure that the multiple images of the aperture code observed on the CCD were horizontal across the face of the CCD and that they were in focus.

A useful technique to approximately determine when the mask was not rotated was to consider plots of the horizontal sum of pixels across the CCD for rows near the top and bottom of the mask images. When the mask was not rotated, there would be a sharp transition in these plots. As the mask was rotated either way, this transition became more gradual. Thus, a quantitative metric to use was to maximize the peak value in the derivative of the plots. In the future, this process could be made much simpler with the use of alignment markers above and/or below the mask patterns.

To focus the mask images on the CCD, the Z-axis on the translational stage was adjusted. A fast Fourier transform (FFT) was performed across a set of CCD columns containing a mask image. The Z-axis position of the translation stage was adjusted until the mean value of the FFT was maximized, corresponding to a maximization of the energy of the high spatial frequencies across the columns of the CCD. This corresponds to a narrower point-spread function for the optical system.

B. Vertical Subpixel Misalignments

A consequence of vertical demagnification and blurring of the optical field and pixelation of the detector array is that when the input aperture is imaged onto the detector, the features do not necessarily impinge on an integral number of pixels. Thus, subpixel misalignments can occur. One of the objectives of this work was to find the aperture code that the MMS spectrometer is least sensitive to in terms of vertical subpixel misalignments on the detector. This translates to studying the effect of subpixel misalignments on the SNR of spectral estimates produced using each aperture code.

An experiment was conducted to test the performance of the spectrometer with each aperture code mask undergoing forced subpixel misalignments. Each mask was twice moved up and down across a CCD pixel in subpixel shifts of 0.1 pixel (roughly 0.9 μm). The final position of the mask was the same as the initial position. Thus, for each mask, a data set of 41 CCD images was taken for conversion to spectra.

Given such a data set, the utility of the forward model development process could be evaluated by checking that the SNR of the spectral estimate for each CCD image in the data set would be the same after the incorporation of the subpixel misalignment into the spectral decoding matrix. Also, the sensitivity of the spectrometer to misalignments of the mask could be evaluated by considering the deterioration of the SNR with increasing subpixel misalignment of the mask images.

The SNR of the spectral reconstruction for a CCD image is maximized when the correct subpixel shift is incorporated into the spectral decoding matrix. Thus, multiple decoding matrices were generated with each incorporating a different amount of subpixel shift ranging from 0 to 10 subpixel shifts of 0.1 pixel (20 simpixels in total). Each CCD image was converted to a spectral estimate with each of these decoding pat-
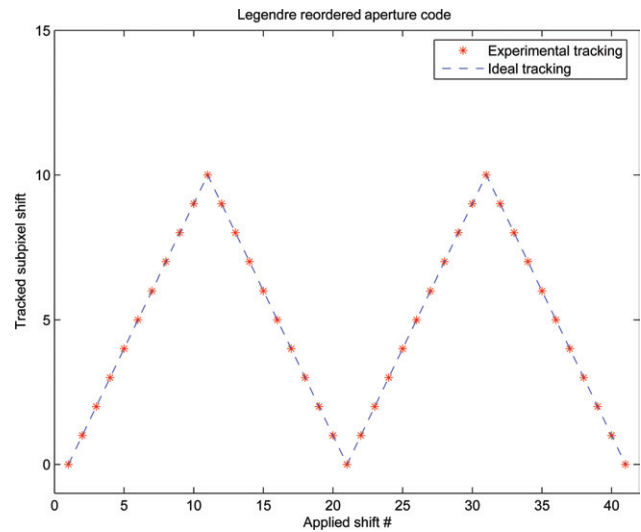

Fig. 19. (Color online) Applied subpixel shift versus tracked subpixel shift. Using the forward model process to incorporate different subpixel shifts into the decoding matrix and choosing the one that maximizes the SNR allows excellent tracking of the applied subpixel shift.

terns and the pattern maximizing the SNR was determined to be the one incorporating the correct subpixel shift. This technique allowed tracking of the 41 forced subpixel shifts of each mask. Figure 19 demonstrates tracking of the forced subpixel shifts of the half-toned, reordered Legendre aperture mask.

With the ability to track subpixel shifts, vertical subpixel misalignments of the mask images on the CCD could be corrected for. Figure 20 shows a plot of SNR versus the applied subpixel misalignment of the half-toned, reordered Legendre aperture code. As ex-
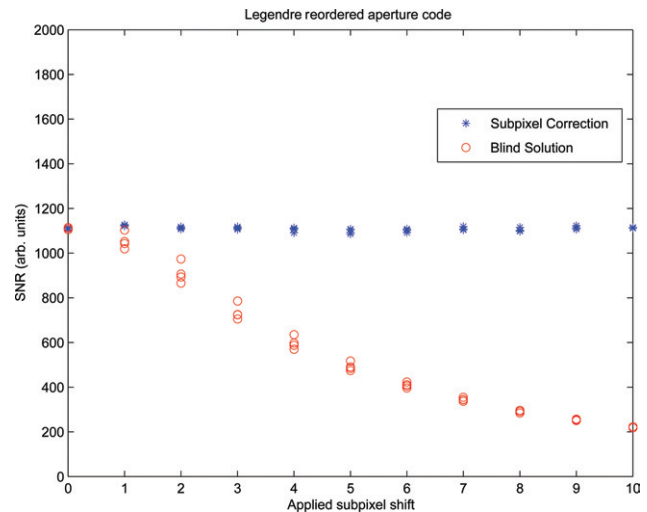

Fig. 20. (Color online) SNR versus applied subpixel shift. The subpixel correction plot demonstrates that incorporating subpixel shifts into the decoding matrix results in the ability to reconstruct spectra with the same SNR at any vertical subpixel misalignment of the aperture images on the detector. When subpixel shifts are not incorporated into the decoding matrix, the SNR degrades with increasing subpixel misalignment.
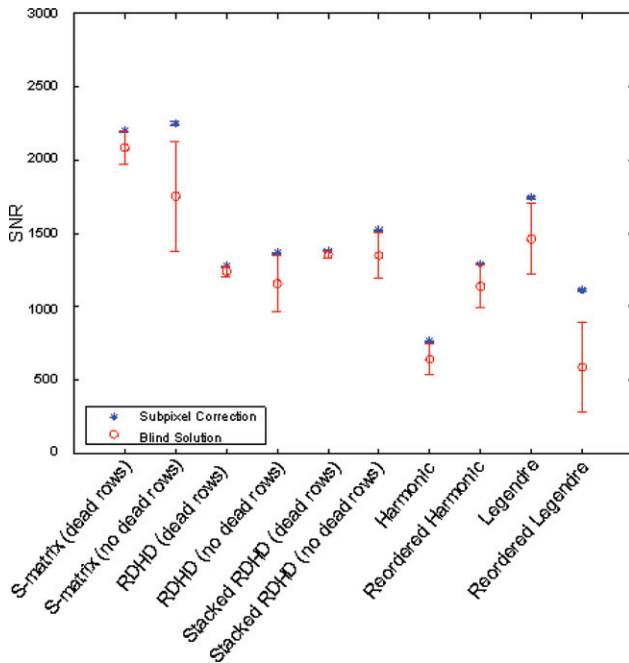
Fig. 21. (Color online) Mean SNR versus mask type. The error bars indicate standard deviation. The *S*-matrix aperture codes produce spectral estimates with the highest SNR. Discrete codes without dead rows have higher mean SNRs than their counterparts containing dead rows. The addition of dead rows decrease the sensitivity of the spectrometer to vertical subpixel misalignments. RDHD, row-doubled Hadamard.

rows. This can be explained by the fact that they transmit more light, thus increasing the amount of photons (or signal) incident on the detector in the presence of noise.

3. On the other hand, the addition of dead rows reduced the spread of SNR values, making a spectrometer with one of these codes less sensitive to vertical subpixel misalignments than a spectrometer containing a code without dead rows. Thus, in addition to reducing cross talk between rows in the code, the dead rows also decrease the sensitivity of the spectrometer to vertical subpixel misalignments.

4. Dead rows in discrete codes are not necessary because subpixel misalignments can be successfully accounted for, as shown in Fig. 20. Thus, the system can benefit by using an aperture code without dead rows that allows greater transmission of light to the detector and an overall higher SNR.

Figure 22 plots the peak-to-peak SNR versus the maximum SNR for the blind solution for each aperture code. The higher the value, the greater the sensitivity of the spectrometer to subpixel misalignments of an aperture code. This plot suggests that the row-doubled Hadamard and the stacked row-doubled Hadamard codes are almost completely insensitive to vertical subpixel misalignments. The stacked code performs better since it has lower spatial frequencies vertically. In general, not correcting for subpixel shifts in the decoding matrix affects the discrete codes with dead rows lesser than it affects the continuous codes. Thus, as far as

pected, allowing for subpixel correction of the decoding pattern gives approximately the same SNR at any applied subpixel misalignment. The blind solution plots the SNR if all 41 images are converted to spectra with the decoding matrix that gives the maximum SNR at the initial mask position. The figure clearly shows that with increasing subpixel misalignments, the SNR degrades and that correcting for the misalignments can significantly improve the SNR.

The above process was repeated for the measured data set of each aperture code. Figure 21 shows a plot of the mean SNR and the spread of SNR values with and without subpixel shift correction for each code. As expected, the spread of SNR values after subpixel shift correction is very low.

A number of conclusions can be drawn from this figure:

1. The *S*-matrix discrete aperture code without dead rows gives us the highest SNR after correcting for subpixel shifts. Ideally, the SNR for both the *S*-matrix and Hadamard codes should be identical. However, the experimental result can be attributed to the modulation transfer function (MTF) of the system. The MTF is lower for the row-doubled Hadamard-based codes than for the *S*-matrix codes because they have greater spatial frequencies vertically.

2. In general, after correcting for subpixel shifts, the discrete codes without dead rows produced higher mean SNRs than their counterparts containing dead
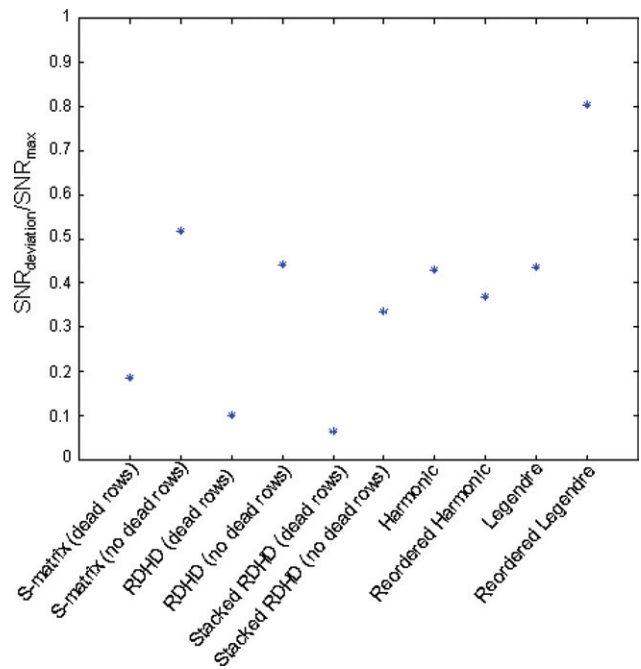

Fig. 22. (Color online) Fractional SNR deviation with 1 pixel misalignment of each aperture code. The discrete codes with dead rows perform considerably better than any of the continuous column codes. The addition of dead rows to a discrete code greatly decreases the sensitivity of the spectrometer to vertical subpixel misalignments of the aperture images on the detector.

vertical subpixel misalignments are concerned, discrete codes are superior to continuous codes.

C. Coded Aperture versus Slit

When compared with a slit-based spectrometer, the use of a coded aperture makes the instrument far more sensitive to weak spectral features [11]. To test this hypothesis, a neutral-density filter of optical density (OD) 1.0 was introduced between the spectrometer and the xenon gas discharge lamp. Then, the stacked row-doubled Hadamard aperture code with dead rows was placed in the spectrometer. Multiple CCD measurements were collected at exposure times ranging from 130 to 2490 ms in steps of 20 ms for a total of 119 measurements. This procedure was repeated with the slit.

Figure 23 plots the reconstructed spectra at increasing exposure times for the coded aperture and the slit. It is clear that the coded aperture mask is much more sensitive to the four major spectral peaks of xenon than the slit. The mask is able to identify the weaker peaks at much lower exposure times. Furthermore, the slit reconstructions are increasingly adversely affected by stray light from the reflective grating at the higher exposure times, as demonstrated by the bright regions between 860–880 and 915–930 nm.

8. Summary

Forward model development was used to determine the parameters for the propagation of the optical field through a coded aperture spectrometer and consequently improve the quality of spectral estimates. Using this technique, the performance of a static MMS coded aperture spectrometer was studied with ten different independent, column coded aperture masks. The use of the discrete S-matrix aperture codes produced spectra with the highest SNR, whereas the stacked row-doubled Hadamard code with dead rows was the least sensitive to vertical subpixel misalignments of the mask images on the detector. Finally, spectral estimates from a coded aperture spectrometer were compared with those from a slit spectrometer to demonstrate the greater sensitivity of a coded-aperture-based instrument.
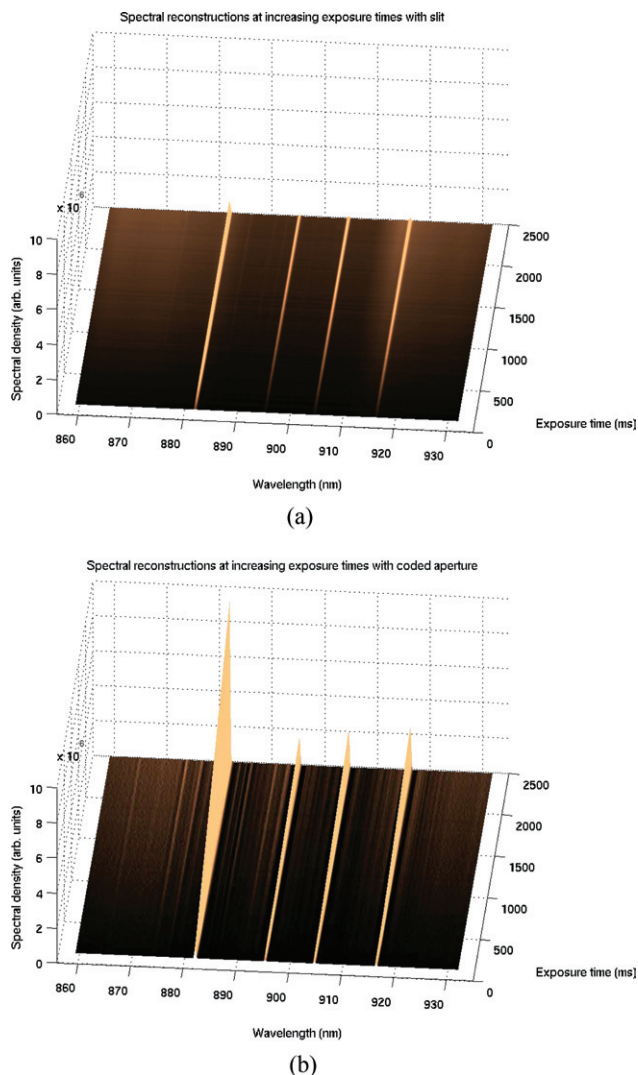
Fig. 23. (Color online) (Top) Spectra reconstructed with slit at increasing exposure times. (Bottom) Spectra reconstructed with coded aperture at increasing exposure times. The coded aperture makes the spectrometer considerably more sensitive to the spectral peaks of xenon in the spectral range of the instrument.

References

1. S. B. Mende, E. S. Claflin, R. L. Rairden, and G. R. Swenson, "Hadamard spectroscopy with a 2-dimensional detecting array," Appl. Opt. **32,** 7095–7105 (1993).
2. M. E. Gehm, S. T. McCain, N. P. Pitsianis, D. J. Brady, P. Potuluri, and M. E. Sullivan, "Static 2D aperture coding for multimodal multiplex spectroscopy," Appl. Opt. **45,** 2857–3183 (2006).
3. S. McCain, M. Gehm, Y. Wang, N. Pitsianis, and D. Brady, "Coded aperture Raman spectroscopy for quantitative measurements of ethanol in a tissue phatom," Appl. Spectrosc. **60,** 663–671 (2006).
4. J. A. Decker and M. O. Harwitt, "Sequential encoding with multislit spectrometers," Appl. Opt. **7,** 2205–2209 (1968).
5. M. Harwit and N. Sloane, *Hadamard Transform Optics* (Academic, 1979), pp. 50–59.
6. D. Schroeder, *Astronomical Optics* (Academic, 1987).
7. C. Lawson and R. Hanson, *Solving Least Squares Problems* (Prentice-Hall, 1974).
8. Y. Zhou and C. K. Rushforth, "Least-squares reconstruction of spatially limited objects using smoothness and non-negativity constraints," Appl. Opt. **21,** 1249–1252 (1982).
9. A. Tarantola, *Inverse Problem Theory and Methods for Model Parameter Estimation* (Society for Industrial and Applied Mathematics, 2005).
10. L. Pan, D. Edwards, J. Gille, M. Smith, and J. Drummond, "Satellite remote sensing of tropospheric CO_2 and CH_4: forward model studies of the MOPITT instrument," Appl. Opt. **34,** 6976–6988 (1995).
11. J. A. Decker, "Experimental realization of multiplex advantage with a Hadamard transform spectrometer," Appl. Opt. **10,** 510–514 (1971).